JACS
JOURNAL OF THE AMERICAN CHEMICAL SOCIETY
Article
pubs.acs.org/JACS

Mechanism Switching of Ammonia Synthesis Over Ru-Loaded Electride Catalyst at Metal–Insulator Transition

Shinji Kanbara,[†,⊥] Masaaki Kitano,[‡,⊥] Yasunori Inoue,[†] Toshiharu Yokoyama,[‡,∥] Michikazu Hara,*[,†,§,∥] and Hideo Hosono*[,†,‡,§,∥]

[†]Materials and Structures Laboratory, Tokyo Institute of Technology, 4259 Nagatsuta, Midori-ku, Yokohama 226-8503, Japan
[‡]Materials Research Center for Element Strategy, Tokyo Institute of Technology, 4259 Nagatsuta, Midori-ku, Yokohama 226-8503, Japan
[§]Frontier Research Center, Tokyo Institute of Technology, 4259 Nagatsuta, Midori-ku, Yokohama 226-8503, Japan
[∥]ACCEL, Japan Science and Technology Agency, 4-1-8 Honcho, Kawaguchi, Saitama, 332-0012, Japan

Supporting Information

ABSTRACT: The substitution of electrons for O^{2-} anions in the crystallographic cages of $[Ca_{24}Al_{28}O_{64}]^{4+}(O^{2-})_2$ was investigated to clarify the correlation between the electronic properties and catalytic activity for ammonia synthesis in Ru-loaded $[Ca_{24}Al_{28}O_{64}]^{4+}(O^{2-})_{2-x}(e^-)_{2x}$ $(0 \le x \le 2)$. This catalyst has low catalytic performance with an electron concentration (N_e) lower than 1×10^{21} cm^{-3} and a high apparent activation energy (E_a) for ammonia synthesis comparable to that for conventional Ru-based catalysts with a basic promoter such as alkali or alkaline earth compounds. Replacement of more than half of the cage O^{2-} anions with electrons ($N_e \approx 1 \times 10^{21}$ cm^{-3}) significantly changes the reaction mechanism to yield a catalytic activity that is an order higher and with half the E_a. The metal–insulator transition of $[Ca_{24}Al_{28}O_{64}]^{4+}(O^{2-})_{2-x}(e^-)_{2x}$ also occurs at $N_e \approx 1 \times 10^{21}$ cm^{-3} and is triggered by structural relaxation of the crystallographic cage induced by the replacement of O^{2-} anions with electrons. These observations indicate that the metal–insulator transition point is a boundary in the catalysis between Ru-loaded $[Ca_{24}Al_{28}O_{64}]^{4+}(O^{2-})_2$ and $[Ca_{24}Al_{28}O_{64}]^{4+}(e^-)_4$. It is thus demonstrated that whole electronic properties of the support material dominate catalysis for ammonia synthesis.

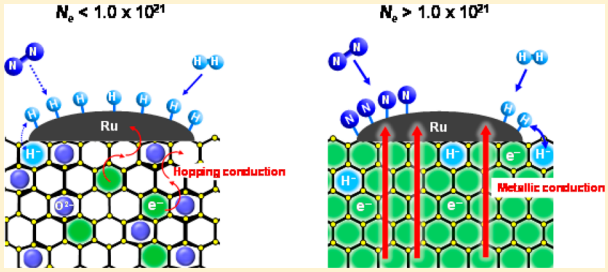

INTRODUCTION

Ammonia synthesis is one of the most important catalytic processes in chemical industry. Since the industrial Haber and Bosch process,[1] promoted iron catalysts have been used in the practical synthesis of ammonia.[2] Ruthenium (Ru)-based catalysts are viable candidates for next-generation ammonia synthesis catalysts because they work under milder conditions than those for the Haber–Bosch process.[3,4] It is well-known that ammonia synthesis on Ru catalyst is a structure-sensitive reaction, i.e., the step sites on Ru (so-called B_5-type step site) exhibit much higher activity in N_2 dissociation than the terrace sites.[5] Decrease in Ru particle size increases the step sites, and the optimal Ru particle size has been theoretically and experimentally demonstrated to be in the range 1.8–3.5 nm.[6−9] In addition, the catalytic activity of Ru catalyst is significantly enhanced by the addition of a basic promoter such as alkali or alkaline earth compounds (Cs^+, K^+, Ba^{2+}, etc.).[3,10−12] The promoter itself is completely inactive in ammonia synthesis but boosts the reaction on Ru metal. This promotion effect is commonly explained by the injection of electrons from the promoter to the antibonding π^*-orbital of N_2 through the Ru catalyst (electronic promoting effect).[4,13,14] Transmission electron microscopic (TEM) observation and chemisorption experiments have revealed that these promoters are located in the vicinity of Ru catalyst,[10,15,16] leading to efficient electron transfer from the promoter to the Ru. On the other hand, some researchers have postulated that a Ba promoter modifies the local arrangement of surface Ru atoms and creates highly active B_5-type sites (structural promoting effect).[12,17,18] In any case, the rate-determining step for ammonia synthesis is N_2 dissociation on the catalyst surface.

We have recently reported that the $12CaO{\cdot}7Al_2O_3$ electride ($C12A7{:}e^-$)[19] functions as an efficient electron donor for a Ru catalyst in ammonia synthesis.[20,21] The unit cell of $C12A7{:}e^-$ can be expressed as $[Ca_{24}Al_{28}O_{64}]^{4+}(e^-)_4$, where the four e^- (extra-framework electrons) are incorporated as counteranions for the positively charged $[Ca_{24}Al_{28}O_{64}]^{4+}$ lattice framework composed of 3-dimensionally connected subnanometer-sized cages. The theoretical maximum exchange (electron concentration (N_e) = 2.3×10^{21} cm^{-3}) results in high electrical conductivity (1500 S cm^{-1}) and a small work function (2.4 eV) comparable to that of metallic K.[19,22] Ru nanoparticle-loaded $[Ca_{24}Al_{28}O_{64}]^{4+}(O^{2-})_2$ (Ru/$C12A7{:}O^{2-}$), in which O^{2-} ions

Received: September 29, 2015
Published: October 24, 2015

DOI: 10.1021/jacs.5b10145
J. Am. Chem. Soc. 2015, 137, 14517−14524

are incorporated in the cages instead of electrons, has catalytic performance similar to conventional Ru-based catalysts available for ammonia synthesis, where the dissociative adsorption of N_2 molecules on Ru/C12A7:O^{2-} is the rate-determining step, as with all heterogeneous ammonia synthesis catalysts reported to date.[21] In addition, even hydrogen poisoning, a common drawback of Ru-based catalysts where hydrogen adatoms prevent ammonia synthesis on Ru surfaces,[11,23] is observed on Ru/C12A7:O^{2-}. In contrast, the dissociative adsorption of N_2 molecules over Ru nanoparticle-loaded C12A7:e^- (Ru/C12A7:e^-) requires a much smaller activation energy (E_a; approximately half) than that for successive processes. Kinetic analyses of exchange reactions between $^{14}N_2$ and $^{15}N_2$ over this catalyst have indicated that the dissociation of N_2 molecules is no longer the rate-determining step on Ru/C12A7:e^-.[21] Ru/C12A7:e^- is also distinct from Ru/C12A7:O^{2-} in that the electride catalyst is not subject to hydrogen poisoning. As a consequence, Ru/C12A7:e^- exhibits much higher catalytic activity for ammonia synthesis under elevated H_2 pressures than other catalysts. These features originate from the following two properties of C12A7:e^-: (1) the electride with a small work function (ca. 2.4 eV) donates electrons to Ru nanoparticles, and the resulting Ru nanoparticles with higher Fermi level inject electrons into the antibonding π^*-orbitals of N_2 molecules; and (2) extra-framework electrons on the C12A7:e^- surfaces react with H adatoms generated on Ru to form extra-framework H^- ions, and this reaction occurs reversibly by varying the partial H_2 pressure and temperature.

Catalysis for most materials and molecules is discussed on the basis of local structure and local electronic state around the active site. However, a striking distinction in the catalysis and electronic properties between Ru/C12A7:O^{2-} and Ru/C12A7:e^- suggests that the total electronic state of the material dominates the ammonia synthesis reaction. In the present study, $[Ca_{24}Al_{28}O_{64}]^{4+}(O^{2-})_{2-x}(e^-)_{2x}$ species with various N_e in the range 0–2.0 × 10^{21} cm^{-3} were prepared to clarify the correlation of N_e for ammonia synthesis Ru/$[Ca_{24}Al_{28}O_{64}]^{4+}(O^{2-})_{2-x}(e^-)_{2x}$ as the catalyst. We also focus on the difference in the electronic promoting effect between C12A7:e^- and a conventional basic promoter such as cesium oxide.

RESULTS

Electron Concentration and Electronic Properties of $[Ca_{24}Al_{28}O_{64}]^{4+}(O^{2-})_{2-x}(e^-)_{2x}$. Figure 1A shows UV–vis absorption spectra for $[Ca_{24}Al_{28}O_{64}]^{4+}(O^{2-})_{2-x}(e^-)_{2x}$ powders with various N_e. The powders were diluted with dehydrated MgO powder in a weight ratio of 1:10. The color of the samples was changed from white to green, to dark brown, to black as N_e was increased from 0 to 2.0 × 10^{21} cm^{-3} (Figure 1B), which is consistent with the colors of C12A7 single crystals treated with Ca metal in a vacuum.[24] $[Ca_{24}Al_{28}O_{64}]^{4+}(O^{2-})_2$ has no absorption band in the visible region, and the absorption edge appears at ca. 3.5 eV, which is due to the excitation between the energy level of encaged O^{2-} ions and the cage conduction band (CCB).[25] In contrast, $[Ca_{24}Al_{28}O_{64}]^{4+}(O^{2-})_{2-x}(e^-)_{2x}$ powders exhibit broad absorption bands at 2–3.5 eV and below 2 eV. The former corresponds to an intracage s-to-p transition of electrons trapped in the cages, and the latter is attributed to an intercage s-to-s transition,[26] i.e., charge transfer from an electron-trapped cage to a vacant neighboring cage.[27] The absorption band

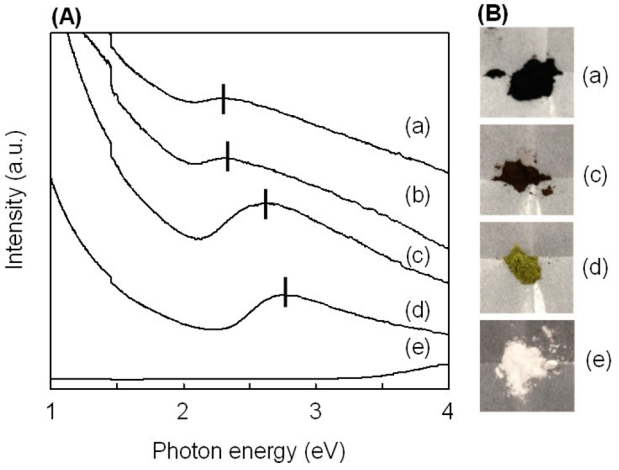

Figure 1. (A) UV–vis absorption spectra (obtained by Kubelka–Munk transformation of diffuse reflectance spectra) for $[Ca_{24}Al_{28}O_{64}]^{4+}(O^{2-})_{2-x}(e^-)_{2x}$ with various electron concentrations of (a) N_e = 2.0 × 10^{21} cm^{-3}, (b) N_e = 1.5 × 10^{21} cm^{-3}, (c) N_e = 0.77 × 10^{21} cm^{-3}, (d) N_e = 0.09 × 10^{21} cm^{-3}, and (e) N_e = 0 cm^{-3} ($[Ca_{24}Al_{28}O_{64}]^{4+}(O^{2-})_2$). The vertical bar indicates the absorption peak position (E_{SP}). (B) Photographs of the synthesized powders.

below 2 eV is broadened, and the band tail extends to larger energies, which is affected by the disorder of the extra-framework species (the details of the lattice distortion induced by extra-framework species are described in the following sections). It was therefore confirmed that O^{2-} ions accommodated in the cages of $[Ca_{24}Al_{28}O_{64}]^{4+}(O^{2-})_2$ are replaced by electrons by heat treatment with Ca or Ti metal in a vacuum. The peak position (E_{sp}) shifts to the lower energy side with increasing N_e. N_e can be estimated from E_{sp} using the experimentally obtained relation of $N_e = [-(E_{sp} - E_{sp}^{\circ})/0.199]^{0.782}$, where the low-$N_e$ limit E_{sp}° = 2.83 eV at $N_e \approx 1 \times 10^{18}$ cm^{-3}.[28] Table 1 shows that the values obtained correspond well with those determined by the iodometric titration method.[29]

Table 1. Electron Concentration (N_e) of $[Ca_{24}Al_{28}O_{64}]^{4+}(O^{2-})_{2-x}(e^-)_{2x}$

N_e[a] (10^{21} cm^{-3})	N_e[b] (10^{21} cm^{-3})
2.00	2.06
1.50	1.87
0.77	0.88
0.09	0.09
0	0

[a]N_e was determined by iodometric titration method. [b]N_e was determined by the relation of $N_e = [-(E_{sp} - E_{sp}^{\circ})/0.199]^{0.782}$.

The electronic structures of $[Ca_{24}Al_{28}O_{64}]^{4+}(O^{2-})_{2-x}(e^-)_{2x}$ with and without electrons are illustrated in Figure 2. The top of the framework valence band (FVB) and the bottom of the framework conduction band (FCB) are composed of the 2p orbitals of the framework O^{2-} ions and the 4s orbitals of the framework Ca^{2+} ions, respectively.[30] The 2p levels of O^{2-} ions in the cages are located in an energy region at ca. 1 eV above the top of the FVB. Furthermore, the CCB derived from electron tunneling among the three-dimensionally connected cages with positive charges is formed in the band gap and is located at 1–2 eV below the FCB. When N_e is lower than 1.0 × 10^{21} cm^{-3}, electrons are confined in the cages and form F^+-like

DOI: 10.1021/jacs.5b10145
J. Am. Chem. Soc. 2015, 137, 14517–14524

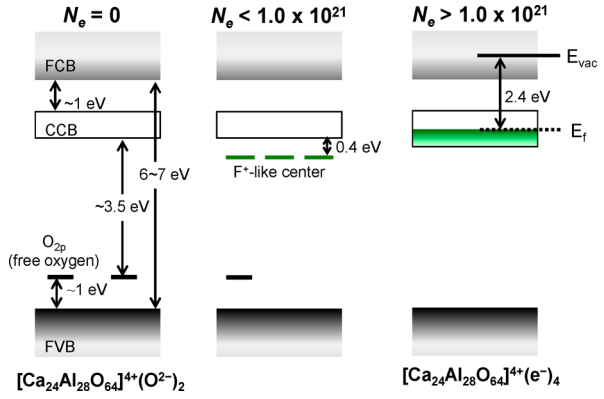

Figure 2. Schematic diagram of the electronic structures of $[Ca_{24}Al_{28}O_{64}]^{4+}(O^{2-})_{2-x}(e^-)_{2x}$ with various N_e. FCB and FVB are the framework conduction band and framework valence band, respectively. CCB denotes the cage conduction band arising from electron-tunneling through the monolayer oxide layers that connect adjacent cages. Note that the Fermi level in the electride exceeds the bottom of the CCB, which indicates the metallic state.

centers of which the energy level is located at 0.4 eV below the CCB.[24] The Fermi energies (E_f's) of $[Ca_{24}Al_{28}O_{64}]^{4+}(O^{2-})_{2-x}(e^-)_{2x}$ with high electron concentrations ($N_e > 1.0 \times 10^{21}$ cm^{-3}) vary from 0.15 to 0.5 eV above the CCB minimum with increasing N_e, which indicates that most of the electrons occupy the delocalized CCB states. The red-shift of the visible absorption peak at 2−3 eV in Figure 1A with N_e is due primarily to the upshift of the Fermi level, which is determined by the 1s level of electrons trapped in the cages.

Figure 3 shows XRD patterns of $[Ca_{24}Al_{28}O_{64}]^{4+}(O^{2-})_{2-x}(e^-)_{2x}$ with various N_e. All samples have mayenite-

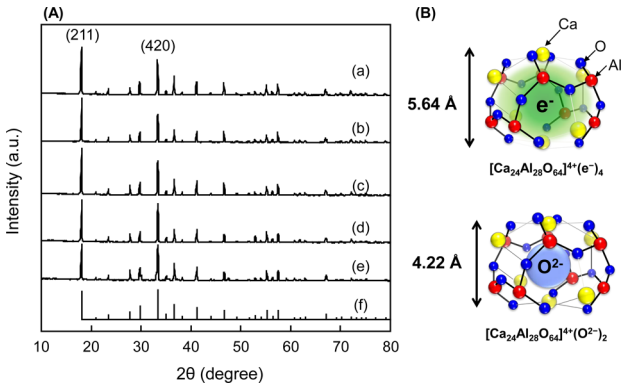

Figure 3. Structural information for C12A7. (A) XRD patterns for $[Ca_{24}Al_{28}O_{64}]^{4+}(O^{2-})_{2-x}(e^-)_{2x}$ with various electron concentrations of (a) $N_e = 2.00 \times 10^{21}$ cm^{-3}, (b) $N_e = 1.50 \times 10^{21}$ cm^{-3}, (c) $N_e = 0.77 \times 10^{21}$ cm^{-3}, (d) $N_e = 0.09 \times 10^{21}$ cm^{-3}, and (e) $N_e = 0$ cm^{-3}. (f) Standard diffraction pattern (PDF 00-009-0413) for mayenite ($Ca_{12}Al_{14}O_{33}$). (B) Geometrical structures of the cages and the corresponding Ca−Ca distances for $[Ca_{24}Al_{28}O_{64}]^{4+}(e^-)_4$ and $[Ca_{24}Al_{28}O_{64}]^{4+}(O^{2-})_2$. Note that the cage geometry distinctly approaches a symmetric shape when extra-framework O^{2-} anions are replaced by electrons.

type structure (space group $I\bar{4}3d$), and no impurity phases were observed in these patterns, which indicates that the visible light absorption in Figure 1 is not due to the presence of impurities. It should be noted that the intensity ratio of the 211 diffraction peak to the 420 diffraction peak increases with N_e. Table S1 summarizes the lattice constants of $[Ca_{24}Al_{28}O_{64}]^{4+}(O^{2-})_{2-x}(e^-)_{2x}$. The lattice constant of $[Ca_{24}Al_{28}O_{64}]^{4+}(O^{2-})_2$ was determined as 11.986 Å, which is in agreement with that reported.[31] In contrast, the $[Ca_{24}Al_{28}O_{64}]^{4+}(O^{2-})_{2-x}(e^-)_{2x}$ samples have slightly larger values, which suggests that the cage structure is expanded by the replacement of O^{2-} with e^- (Figure 3B). This is due to the stronger interaction between encaged O^{2-} ions and axial Ca^{2+} ions than that with electrons.[32] As a consequence, the separation between two Ca^{2+} ions in the cage poles (D_{ax}) increases from 4.22 Å ($[Ca_{24}Al_{28}O_{64}]^{4+}(O^{2-})_2$) to 5.64 Å ($[Ca_{24}Al_{28}O_{64}]^{4+}(e^-)_4$), as demonstrated by electron density analysis with application of the maximum entropy Rietveld method.[32]

Catalysis of Ru-Loaded $[Ca_{24}Al_{28}O_{64}]^{4+}(O^{2-})_{2-x}(e^-)_{2x}$. Figure 4 shows scanning TEM (STEM) images of Ru-loaded

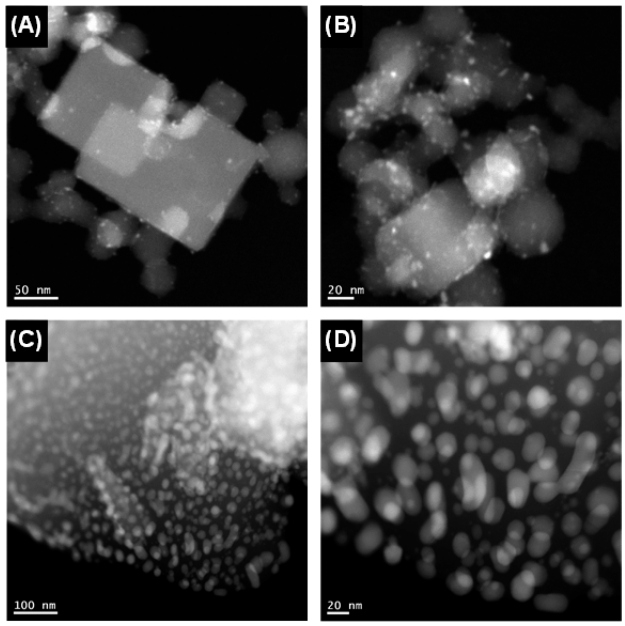

Figure 4. High angle annular dark field (HAADF) STEM images of (A, B) Ru(2 wt %)−Cs/MgO and (C, D) Ru(2 wt %)/$[Ca_{24}Al_{28}O_{64}]^{4+}(e^-)_{2x}$. These samples are reduced under N_2 and H_2 flow (N_2:H_2 = 1:3) at 400 °C before observation.

$[Ca_{24}Al_{28}O_{64}]^{4+}(e^-)_{2x}$ and Ru−Cs/MgO catalysts. Small Ru nanoparticles (<5 nm) are dispersed on Ru−Cs/MgO. This particle size is close to those in the previous literature.[10,11,16] On the other hand, large round-shaped Ru particles are deposited on Ru/$[Ca_{24}Al_{28}O_{64}]^{4+}(e^-)_{2x}$. Although small Ru nanoparticles (3−5 nm) are also observed on the electride catalyst, most of the Ru particles are much larger than 10 nm. Because of the small surface area of $[Ca_{24}Al_{28}O_{64}]^{4+}(e^-)_{2x}$, Ru particles easily aggregate with each other on the surface during the deposition process or reducing treatment under hydrogen atmosphere. Ru particle sizes observed by STEM images are consistent with average Ru particle sizes estimated by CO chemisorption (Table 2) for Ru−Cs/MgO and Ru/$[Ca_{24}Al_{28}O_{64}]^{4+}(e^-)_{2x}$. The optimum Ru particle size for ammonia synthesis has been reported to be in the range 1.8−3.5 nm because the relative number of the active sites (B_5-type step sites) increases with decreasing Ru particle size, reaching a maximum at ~2 nm.[6−9] Therefore, it can be considered that large Ru particles on $[Ca_{24}Al_{28}O_{64}]^{4+}(e^-)_{2x}$ are not suitable for efficient ammonia synthesis. However, Ru/

DOI: 10.1021/jacs.5b10145
J. Am. Chem. Soc. 2015, 137, 14517−14524

Table 2. Characterization and Activity of Various Ru (2 wt %)-Loaded Supports for Ammonia Synthesis

catalyst	N_e[a] (10^{21} cm^{-3})	S_{BET}[b] (m^2 g^{-1})	dispersion[c] (%)	particle size[c] (nm)	r_{NH_3}[d] (mmol g^{-1} h^{-1})	TOF[e] (s^{-1})	E_a[f] (kJ mol^{-1})
Ru/$[Ca_{24}Al_{28}O_{64}]^{4+}(O^{2-})_{2-x}(e^-)_{2x}$	2.00	1.0	4.7	28.7	3.02	0.10	50
	1.50	1.0	4.6	29.3	2.61	0.09	59
	1.00	1.0	4.9	26.5	3.02	0.10	48
	0.77	1.0	4.1	32.9	1.11	0.04	83
	0.50	1.0	4.6	29.4	0.27	0.01	113
	0.09	0.7	3.5	37.5	0.15	0.01	97
Ru/$[Ca_{24}Al_{28}O_{64}]^{4+}(O^{2-})_2$	0	1.0	3.9	34.9	0.23	0.01	104
Ru−Cs/$[Ca_{24}Al_{28}O_{64}]^{4+}(O^{2-})_2$	0	1.0	3.9	34.9	0.60	0.02	113
Ru−Cs/MgO		12	25.4	2.5	2.66	0.01	100

[a]Electron concentration of $[Ca_{24}Al_{28}O_{64}]^{4+}(O^{2-})_{2-x}(e^-)_{2x}$. [b]Surface area. [c]Dispersion and particle size were calculated on the basis of CO chemisorption values, assuming spherical metal particles and the stoichiometry of Ru/CO = 1. [d]NH_3 synthesis rate: synthesis gas (H_2/N_2 = 3/60 mL min^{-1}), reaction temperature (360 °C), pressure (0.1 MPa). [e]TOF (turnover frequency) was calculated from the reaction rate divided by the number of CO atoms chemisorbed on the Ru surfaces. [f]Activation energy was calculated from Arrhenius plots of the reaction rate in the temperature range 340−400 °C.

$[Ca_{24}Al_{28}O_{64}]^{4+}(e^-)_{2x}$ exhibits high catalytic performance for ammonia synthesis. This result is attributable to strong electron-donation capability as described below.

The catalytic performance of Ru/$[Ca_{24}Al_{28}O_{64}]^{4+}(O^{2-})_{2-x}(e^-)_{2x}$ with various N_e was evaluated according to ammonia synthesis at atmospheric pressure. Figure 5 shows the

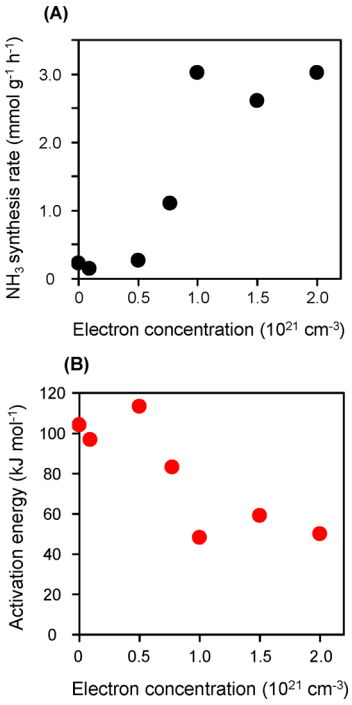

Figure 5. (A) Ammonia synthesis rate and (B) activation energy with Ru-loaded $[Ca_{24}Al_{28}O_{64}]^{4+}(O^{2-})_{2-x}(e^-)_{2x}$ catalysts as a function of electron concentration. Reaction conditions: catalyst (0.1 g), synthesis gas (H_2/N_2 = 3/60 mL min^{-1}), reaction temperature (360 °C), and total pressure (0.1 MPa).

catalytic activity and the E_a of Ru/$[Ca_{24}Al_{28}O_{64}]^{4+}(O^{2-})_{2-x}(e^-)_{2x}$ for ammonia synthesis. The surface area, Ru dispersion, mean Ru particle diameter, turnover frequency (TOF), and E_a are also summarized in Table 2. The catalytic activity for ammonia synthesis remains unchanged with increasing N_e up to 0.5 × 10^{21} cm^{-3}. N_e beyond 0.5 × 10^{21} cm^{-3} largely increases the ammonia synthesis rate and reaches a plateau at ca. 1.0 × 10^{21} cm^{-3}. Ru/$[Ca_{24}Al_{28}O_{64}]^{4+}(O^{2-})_{2-x}(e^-)_{2x}$ with N_e = 2.0 × 10^{21} cm^{-3}, which is very close to the theoretical maximum N_e (2.3 × 10^{21} cm^{-3}, corresponding to the total positive charge of the cage walls), exhibits catalytic activity an order higher than Ru/$[Ca_{24}Al_{28}O_{64}]^{4+}(O^{2-})_{2-x}(e^-)_{2x}$ with $N_e \leq 0.5 \times 10^{21}$ cm^{-3} at 360 °C, comparable to that of Ru−Cs/MgO catalyst. From a consideration of TOF, Ru/$[Ca_{24}Al_{28}O_{64}]^{4+}(O^{2-})_{2-x}(e^-)_{2x}$ at $N_e \geq 1.0 \times 10^{21}$ cm^{-3} has much higher catalytic performance, even compared with Ru−Cs/MgO. There is no significant difference in surface area, Ru particle size, and dispersion among the Ru/$[Ca_{24}Al_{28}O_{64}]^{4+}(O^{2-})_{2-x}(e^-)_{2x}$ samples, as shown in Table 2, which suggests that the correlation of catalysis with N_e in Ru/$[Ca_{24}Al_{28}O_{64}]^{4+}(O^{2-})_{2-x}(e^-)_{2x}$ is not due to morphological reasons, but to the electronic properties of $[Ca_{24}Al_{28}O_{64}]^{4+}(O^{2-})_{2-x}(e^-)_{2x}$ itself. It should be noted that the correlation of E_a with N_e in Figure 5B is similar to that between the ammonia synthesis rate and N_e, where N_e above 1.0 × 10^{21} cm^{-3} results in a halving of E_a for ammonia synthesis with Ru/$[Ca_{24}Al_{28}O_{64}]^{4+}(O^{2-})_{2-x}(e^-)_{2x}$. This observation suggests that the reaction mechanism over Ru/$[Ca_{24}Al_{28}O_{64}]^{4+}(O^{2-})_{2-x}(e^-)_{2x}$ changes at approximately N_e = 1.0 × 10^{21} cm^{-3}. Ru/$[Ca_{24}Al_{28}O_{64}]^{4+}(O^{2-})_{2-x}(e^-)_{2x}$ at N_e = 0.09−0.5 × 10^{21} cm^{-3} has E_a in the range 100−110 kJ mol^{-1}, which is equivalent to that for Ru/$[Ca_{24}Al_{28}O_{64}]^{4+}(O^{2-})_2$ (104 kJ mol^{-1}). While the rate-determining step for ammonia synthesis over Ru/$[Ca_{24}Al_{28}O_{64}]^{4+}(O^{2-})_2$ is still the dissociative adsorption of N_2 molecules, which is similar to other heterogeneous catalysts reported to date for ammonia synthesis,[33] this process is not the rate-determining step for Ru/$[Ca_{24}Al_{28}O_{64}]^{4+}(e^-)_4$. Highly efficient electron donation of $[Ca_{24}Al_{28}O_{64}]^{4+}(e^-)_4$ through Ru facilitates the cleavage of N_2 molecules, which results in a small E_a for N_2 cleavage below 30 kJ mol^{-1}.[21] As a result, this process becomes immaterial for the entire ammonia synthesis process, and E_a with Ru/$[Ca_{24}Al_{28}O_{64}]^{4+}(e^-)_4$ is ca. 50 kJ mol^{-1} due to the successive processes, including the formation of NH species. E_a values for Ru/$[Ca_{24}Al_{28}O_{64}]^{4+}(O^{2-})_{2-x}(e^-)_{2x}$ with $N_e \geq 1.0 \times 10^{21}$ cm^{-3} are in the range 50−60 kJ mol^{-1}; therefore, N_2 cleavage is not the rate-determining step for ammonia synthesis over Ru/$[Ca_{24}Al_{28}O_{64}]^{4+}(O^{2-})_{2-x}(e^-)_{2x}$.

Alkali metal compounds such as Cs-oxide and K-oxide are used as promoters for Ru catalysts.[3,11,34] Therefore, the catalytic activity of Ru/$[Ca_{24}Al_{28}O_{64}]^{4+}(O^{2-})_2$ modified with Cs-oxide was also verified to compare the electronic promoting effect of C12A7:e$^-$ with conventional alkali promoters. When Cs-oxide

DOI: 10.1021/jacs.5b10145
J. Am. Chem. Soc. 2015, 137, 14517−14524

was added to the surface of Ru/$[Ca_{24}Al_{28}O_{64}]^{4+}(O^{2-})_2$, it exhibited 3-fold higher activity than Ru/$[Ca_{24}Al_{28}O_{64}]^{4+}(O^{2-})_2$ (Table 2). However, the activity is significantly inferior to that of Ru/$[Ca_{24}Al_{28}O_{64}]^{4+}(O^{2-})_{2-x}(e^-)_{2x}$ with high N_e, and the E_a for Ru/$[Ca_{24}Al_{28}O_{64}]^{4+}(O^{2-})_2$ is not lowered by the addition of Cs-oxide. Therefore, it was demonstrated that the electronic promoting effect of C12A7:e^- is much more efficient than that of alkali metal compounds.

The reaction orders with respect to N_2 and H_2 were measured to examine the reaction mechanism of ammonia synthesis over Ru/$[Ca_{24}Al_{28}O_{64}]^{4+}(O^{2-})_{2-x}(e^-)_{2x}$. Figure 6

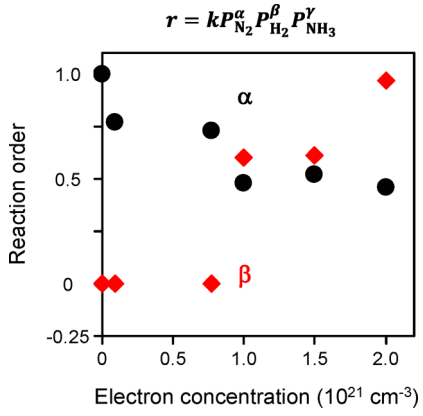

Figure 6. Reaction order with respect to N_2 (black ●) and H_2 (red ◆) for Ru-loaded $[Ca_{24}Al_{28}O_{64}]^{4+}(O^{2-})_{2-x}(e^-)_{2x}$ catalysts as a function of electron concentration. Reaction conditions: catalyst (0.1 g), reaction temperature (360 °C), and total pressure (0.1 MPa).

shows the reaction orders for N_2 at N_e< and ≥1.0×10^{21} cm^{-3} are 0.75−1.0 and ca. 0.5, respectively. The reaction orders for N_2 on conventional catalysts, including Fe- and Ru-based materials, are 0.8−1.0.[35,36] However, the reaction order for N_2 over Ru/C12A7:e^- is ca. 0.5 because N_2 cleavage on Ru/C12A7:e^- is so efficient that this process is not the rate-determining step for ammonia synthesis, and N adatoms populate the Ru/C12A7:e^- surface more densely than the surfaces of other catalysts.[21] Figure 6 thus shows that such highly efficient N_2 cleavage occurs at $N_e \geq 1.0 \times 10^{21}$ cm^{-3}. The reaction order for H_2 is 0 at $N_e < 1.0 \times 10^{21}$ cm^{-3}, which indicates that hydrogen poisoning occurs on Ru, a common and serious drawback with Ru-based catalysts, where the dissociative adsorption of H_2 is preferred over N_2 cleavage on Ru, which inhibits efficient ammonia synthesis under high pressures.[11,23] In contrast, the reaction order becomes positive (0.6−1) when N_e reaches 1.0×10^{21} cm^{-3} or greater. These positive values indicate that Ru/$[Ca_{24}Al_{28}O_{64}]^{4+}(O^{2-})_{2-x}(e^-)_{2x}$ prevents hydrogen poisoning, which can be attributed to the hydrogen storage capability of the material. H atoms spill over from the Ru surface and react with cage electrons in C12A7:e^- near junctions between Ru and C12A7:e^- to form H^- in cages ($H^0 + e^- \rightarrow H^-$). The electrons remain in the cages when H atoms are released from the cages ($H^- \rightarrow H^0 + e^-$).[37] Therefore, not only the rate and E_a for ammonia synthesis but also the reaction mechanism are significantly changed beyond $N_e = 1.0 \times 10^{21}$ cm^{-3}. This N_e corresponds to the critical N_e for the metal−insulator transition in $[Ca_{24}Al_{28}O_{64}]^{4+}(O^{2-})_{2-x}(e^-)_{2x}$.[26]

DISCUSSION

It has been reported that the electrical conduction mechanism of C12A7 varies depending on N_e and the metal−insulator transition occurs at $N_e = 1.0 \times 10^{21}$ cm^{-3}.[26,32] $[Ca_{24}Al_{28}O_{64}]^{4+}(O^{2-})_2$ without electrons in the cages is a typical band insulator. At low N_e (<1.0×10^{21} cm^{-3}), electrons are isolated from each other and localized in the cages, which results in the formation of an F^+-like center energy level at a deep level (Figure 2). The electron localization is strongly correlated with the lattice distortion. As shown in Figure 3B, the lattice distortion is driven by the ionic interaction between the positively charged cage wall and the extra-framework ions, i.e., the values of D_{ax} for cages occupied by O^{2-} and e^- are 4.22 and 5.64 Å, respectively. It is reported that the local geometry of the empty cages remains almost unaffected (D_{ax} = 5.66 Å) when one type of extra-framework ion is replaced by another, and these empty cages function as sites for (intercage) electron hopping.[30] The electron migration requires extra energy (ca. 0.4 eV)[38] because the extra-framework electron forms a polaron that has a strong interaction with the cage framework. Therefore, the lattice distortion provides polaron-type cage-to-cage electron hopping, so that $[Ca_{24}Al_{28}O_{64}]^{4+}(O^{2-})_{2-x}(e^-)_{2x}$ with low N_e (<1.0×10^{21} cm^{-3}) exhibits semiconducting behavior. As the O^{2-} ions are gradually replaced with electrons, the corresponding cage expands and D_{ax} increases from 4.22 to 5.64 Å. This difference leads to relaxation of the lattice cages, and the extra-framework electrons can easily move to an adjacent empty cage without extra energy because the electron−lattice interaction is significantly weakened (no polaron formation).[26] Thus, an extra-framework electron in the cage percolates through the unit cell at $N_e \geq 1.0 \times 10^{21}$ cm^{-3}, which results in metallic conductivity ($d\rho/dT < 0$, where ρ denotes electrical resistivity). In this case, extra-framework electrons occupy the delocalized CCB states (effective mass ca. 1),[26] which accounts for the upshift of the Fermi level (E_f) (Figure 2). These results indicate that the insulator-to-metal transition occurs when more than half of the O^{2-} ions are replaced by electrons.

Table 3 summarizes the catalytic performance of Ru/$[Ca_{24}Al_{28}O_{64}]^{4+}(O^{2-})_{2-x}(e^-)_{2x}$ with higher or lower N_e than

Table 3. Catalytic Performance of Ru/$[Ca_{24}Al_{28}O_{64}]^{4+}(O^{2-})_{2-x}(e^-)_{2x}$ with Various N_e and Ru−Cs/MgO for Ammonia Synthesis[a]

	Ru/$[Ca_{24}Al_{28}O_{64}]^{4+}(O^{2-})_{2-x}(e^-)_{2x}$		Ru−Cs/MgO
N_e (cm^{-3})	≥1.0×10^{21}	<1.0×10^{21}	
TOF (s^{-1})	0.10	0.01	0.01
E_a (kJ mol^{-1})	~50	80−110	100
α	~0.5	0.75−1.0	1.0
β	0.6−1.0	0	−0.43

[a] N_e, electron concentration; TOF, turnover frequency; E_a, activation energy; α and β, the reaction order with respect to N_2 and H_2, respectively.

that of the metal−insulator transition point. There is a striking distinction in catalysis between these two types of Ru/$[Ca_{24}Al_{28}O_{64}]^{4+}(O^{2-})_{2-x}(e^-)_{2x}$ catalysts; i.e., high N_e catalysts exhibit much higher catalytic activity in terms of TOF and almost half the E_a than low N_e catalysts. Furthermore, the reaction order for N_2 decreases from 0.75−1.0 to 0.5, and that for H_2 jumps from 0 to 0.6−1.0 at $N_e \geq 1.0 \times 10^{21}$ cm^{-3}. It is important to note that each catalytic feature of Ru/

DOI: 10.1021/jacs.5b10145
J. Am. Chem. Soc. 2015, 137, 14517−14524

$[Ca_{24}Al_{28}O_{64}]^{4+}(O^{2-})_{2-x}(e^-)_{2x}$ with low N_e is quite similar to that of Ru−Cs/MgO, which indicates that the electronic promoting effect of $[Ca_{24}Al_{28}O_{64}]^{4+}(O^{2-})_{2-x}(e^-)_{2x}$ with low N_e ($<1.0 \times 10^{21}$ cm^{-3}) is almost the same as that of a conventional alkali promoter such as cesium oxide. The clear difference in catalysis with electride catalysts suggests that the dominant reaction pathway is switched at the metal−insulator transition point. One possible explanation for the change in the reaction mechanism at the metal−insulator transition point is the appearance of itinerant electrons in the CCB state of $[Ca_{24}Al_{28}O_{64}]^{4+}(O^{2-})_{2-x}(e^-)_{2x}$. Figure 7 shows the reaction

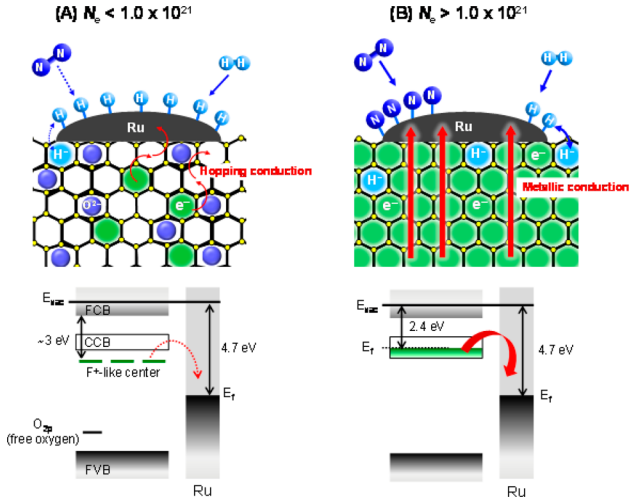

Figure 7. Proposed reaction mechanism for ammonia synthesis over Ru-loaded $[Ca_{24}Al_{28}O_{64}]^{4+}(O^{2-})_{2-x}(e^-)_{2x}$. At (A) low N_e ($<1.0 \times 10^{21}$ cm^{-3}), electrons are localized in the cages due to the lattice distortion induced by extra-framework species, and an F$^+$-like center energy level is formed at the deep position. As a result, the electron-donating ability via polaron-type electron hopping is moderate. H^- ions are also stabilized in the cages by the lattice distortion, which suppresses hydrogen desorption. Hydrogen poisoning then occurs on the Ru surface. At (B) high N_e ($\geq 1.0 \times 10^{21}$ cm^{-3}), electrons are delocalized in the cages because of the weak electron−lattice interaction derived from relaxation of the lattice cages. N_2 dissociation is promoted by efficient electron transfer from the support material because $[Ca_{24}Al_{28}O_{64}]^{4+}(O^{2-})_{2-x}(e^-)_{2x}$ exhibits metallic conductivity and a low work function. The reversible hydrogen storage reaction then proceeds effectively because H^- ions are not stabilized in the homogeneous lattice cage structure, so that N_2 dissociation on the Ru surface is not inhibited by hydrogen adsorption.

mechanism proposed to account for this. At $N_e < 1.0 \times 10^{21}$ cm^{-3}, localized electrons in the cages form an F$^+$-like center energy level at a deep position and electron transfer from $[Ca_{24}Al_{28}O_{64}]^{4+}(O^{2-})_{2-x}(e^-)_{2x}$ to Ru occurs via polaron-type cage-to-cage electron hopping. Accordingly, the electron-donating capability and electron mobility in $[Ca_{24}Al_{28}O_{64}]^{4+}(O^{2-})_{2-x}(e^-)_{2x}$ are largely limited, so that the cleavage of N_2 requires a high E_a and thus remains the rate-determining step for ammonia synthesis as with all conventional heterogeneous catalysts. In addition, Ru/$[Ca_{24}Al_{28}O_{64}]^{4+}(O^{2-})_{2-x}(e^-)_{2x}$ can absorb hydrogen as H^- ions in the cages ($H^0 + e^- \rightarrow H^-$), but the incorporated H^- ions are stabilized in the cages due to the lattice distortion induced by extra-framework species, such as with electrons. This stabilization suppresses the reverse reaction ($H^- \rightarrow H^0 + e^-$), which would result in a dense population of H adatoms on the Ru surfaces loaded on $[Ca_{24}Al_{28}O_{64}]^{4+}(O^{2-})_{2-x}(e^-)_{2x}$. This further limits N_2 cleavage (Figure 7A).

$[Ca_{24}Al_{28}O_{64}]^{4+}(O^{2-})_{2-x}(e^-)_{2x}$ beyond the metal−insulator transition point ($N_e \geq 1.0 \times 10^{21}$ cm^{-3}) exhibits metallic conductivity and a small work function (2.4 eV) because most of the electrons occupy a shallow level of the CCB, and the electron−lattice interaction is weakened by relaxation of the lattice cages (Figure 7B). Such a state enhances electron-donating capability and electron mobility of $[Ca_{24}Al_{28}O_{64}]^{4+}(O^{2-})_{2-x}(e^-)_{2x}$ significantly. These properties facilitate the dissociative adsorption of N_2, so that this process is no longer the rate-determining step for ammonia synthesis. In addition, a high density of electrons in the cages provide reaction sites for hydrogen storage ($H^0 + e^- \rightarrow H^-$), and the H^- ions are readily desorbed from the cages ($H^- \rightarrow H^0 + e^-$) due to the weak interaction between H^- ions and the lattice cages. Such a reversible hydrogen storage reaction decreases H adatoms on the Ru surfaces and produces vacant surface sites for the cleavage of N_2, synergistically accelerating N_2 cleavage.

CONCLUSIONS

The effect of N_e in $[Ca_{24}Al_{28}O_{64}]^{4+}(O^{2-})_{2-x}(e^-)_{2x}$ on the catalytic performance of supported Ru catalysts for ammonia synthesis was demonstrated. When N_e is below 1.0×10^{21} cm^{-3}, electrons are localized in the cages as F$^+$-like centers with the level formed at a deep position, which leads to moderate catalytic activity and a high E_a comparable to that of conventional Ru catalysts such as Ru−Cs/MgO. In this case, N_2 dissociation is the rate-determining step, and strong hydrogen adsorption on the Ru surface prevents the reaction. For $N_e \geq 1.0 \times 10^{21}$ cm^{-3}, electrons are delocalized over the cages of C12A7:e$^-$ and form a shallower electronic level, which results in high catalytic activity and lower E_a. These electronic properties facilitate N_2 dissociation, so that the rate-determining process is changed from N_2 dissociation to N−H bond formation. In addition, a high density of electrons in the cages also enhances a reverse hydrogen storage reaction, which prevents hydrogen poisoning of the Ru surface by hydrogen adatoms. It was demonstrated that the electronic promoting effect of C12A7:e$^-$ in ammonia synthesis is fundamentally different from that of conventional basic promoters such as cesium oxide. The present findings provide important information toward understanding the effect of electronic promoters on the reaction mechanism for ammonia synthesis.

EXPERIMENTAL SECTION

Preparation of C12A7 Catalyst. C12A7:O^{2-} ($[Ca_{24}Al_{28}O_{64}]^{4+}(O^{2-})_2$) powders were synthesized by conventional solid-phase reaction of $CaCO_3$ and α-Al_2O_3 with a molar ratio of 12:7 at 1300 °C for 20 h in ambient air. $[Ca_{24}Al_{28}O_{64}]^{4+}(O^{2-})_{2-x}(e^-)_{2x}$ powders were prepared by the following three methods according to the procedure described in the literature.[26,28,39] The first method is available for the preparation of $[Ca_{24}Al_{28}O_{64}]^{4+}(O^{2-})_{2-x}(e^-)_{2x}$ with a very low N_e (0.09×10^{21} cm^{-3}). C12A7:O^{2-} powders were heated in a carbon crucible with a carbon cap at 1600 °C (partial pressure of O_2: ca. 10^{-16} atm) for 1 h and then slowly cooled to room temperature. This process was repeated twice to obtain $[Ca_{24}Al_{28}O_{64}]^{4+}(O^{2-})_{2-x}(e^-)_{2x}$, where a small part of cage O^{2-} anions are replaced with electrons so that $N_e = 0.09 \times 10^{21}$ cm^{-3}. $[Ca_{24}Al_{28}O_{64}]^{4+}(O^{2-})_{2-x}(e^-)_{2x}$ samples with $N_e = 0.77 \times 10^{21}$ cm^{-3} were prepared using metallic Ti. The pelletized C12A7:O^{2-} (3 g) and Ti metal shot were sealed in a silica glass tube under vacuum and heated at 1000 °C for 20 h. After the reduction treatment, the surface of the sample was mechanically polished to remove the TiO_2 layer

DOI: 10.1021/jacs.5b10145
J. Am. Chem. Soc. 2015, 137, 14517−14524

formed on the surface of the $[Ca_{24}Al_{28}O_{64}]^{4+}(O^{2-})_{2-x}(e^-)_{2x}$ pellet. The $[Ca_{24}Al_{28}O_{64}]^{4+}(O^{2-})_{2-x}(e^-)_{2x}$ pellet was then ground into powder. In the third preparation method, a mixture of C12A7:O^{2-} and $CaO{\cdot}Al_2O_3$ + Ca metal shot to obtain $[Ca_{24}Al_{28}O_{64}]^{4+}(O^{2-})_{2-x}(e^-)_{2x}$ stoichiometry was heated in an evacuated silica tube at 700 °C for 15 h. After the obtained powder was further ground in an Ar glovebox, the sample was reheated in an evacuated silica tube at 1100 °C for 2 h. The mixture of C12A7:O^{2-} and $CaO{\cdot}Al_2O_3$ was prepared by the reaction of $CaCO_3$ and α-Al_2O_3 with molar ratios of 11.75:7, 11.5:7, 11.25:7, and 11:7. These mixed oxide powders were heated with Ca metal shot with weight ratios (Ca metal/mixture of C12A7:O^{2-} and $CaO{\cdot}Al_2O_3$) of 0.015, 0.03, 0.045, and 0.06, which resulted in samples with $N_e = 0.5 \times 10^{21}$, 1.0×10^{21}, 1.5×10^{21}, and 2.0×10^{21} cm^{-3}, respectively. Ru loading was performed by chemical vapor deposition using $Ru_3(CO)_{12}$ (Aldrich) according to a method reported in the literature.[20] Ru−Cs/$[Ca_{24}Al_{28}O_{64}]^{4+}(O^{2-})_2$, where cesium oxide is added as an electron-donating promoter to Ru particles on $[Ca_{24}Al_{28}O_{64}]^{4+}(O^{2-})_2$, was also prepared by the following procedure, which is analogous with the preparation method for Ru−Cs/MgO.[11] Ru/$[Ca_{24}Al_{28}O_{64}]^{4+}(O^{2-})_2$ was dispersed in a solution of Cs_2CO_3 in absolute ethanol by stirring for 3 h, after which the solvent was evaporated and the catalyst was dried in a vacuum. The atomic ratio of Cs/Ru in the catalyst was 1.0.

Characterization of Catalysts. Diffuse reflectance spectra of the samples were measured with a spectrometer (V-670, Jasco). An iodometric titration method was used to confirm the presence of electrons and to estimate N_e in $[Ca_{24}Al_{28}O_{64}]^{4+}(O^{2-})_{2-x}(e^-)_{2x}$.[29] The crystal structure was identified using X-ray diffractometry (XRD; Ultima-IV, Rigaku). The morphology was investigated by scanning transmission electron microscope (STEM; JEM-2100F, JEOL), and high angle annular dark field imaging (HAADF) was used in the STEM mode. N_2 adsorption−desorption isotherms were measured at −196 °C using a specific surface area analyzer (Nova 4200e, Quantachrome) after the sample was evacuated at 300 °C. The Ru dispersion was determined by the CO-pulse chemisorption method using an automatic gas-adsorption apparatus (BELCAT-A, BEL). Prior to CO-pulse chemisorption, the samples were pretreated with a He flow (50 mL min^{-1}) at 400 °C for 15 min, followed by a H_2 flow (50 mL min^{-1}) at 400 °C for 15 min. Hydrogen atoms adsorbed on the reduced catalysts were removed by purging with He (50 mL min^{-1}) at 400 °C for 15 min. The metal dispersion was calculated assuming a stoichiometry of Ru/CO = 1.[40]

Catalysis Evaluation. Catalysis of the samples was evaluated through ammonia synthesis in a fixed-bed continuous-flow reactor containing 0.1 g of the catalyst under ambient pressure (0.1 MPa). The reaction temperature range and the flow rate of a stoichiometric H_2 and N_2 mixture (H_2/N_2 = 3, purity >99.999 95%) were 340−400 °C and 60 mL min^{-1}, respectively. The reaction order with respect to N_2 or H_2 was obtained at a constant flow rate (60 mL min^{-1}) using Ar gas as a diluent, and that for NH_3 was determined with ($3H_2 + N_2$) by changing the synthesis gas flow rate.[36] The ammonia produced was trapped in a 5 mM H_2SO_4 aqueous solution, and the amount of NH_4^+ in the solution was determined using an ion chromatograph (LC-2000 plus, Jasco) equipped with a conductivity detector.

■ ASSOCIATED CONTENT

Supporting Information

The Supporting Information is available free of charge on the ACS Publications website at DOI: 10.1021/jacs.5b10145.

Lattice constants of the materials (PDF)

■ AUTHOR INFORMATION

Corresponding Authors

*mhara@msl.titech.ac.jp

*hosono@msl.titech.ac.jp

Author Contributions

⊥S.K. and M.K. contributed equally.

Notes

The authors declare no competing financial interest.

■ ACKNOWLEDGMENTS

The authors appreciate the technical assistance provided by M. Okunaka, S. Fujimoto, E. Sano, and Y. Takasaki. We thank T. Komanoya for performing STEM measurements. This work was supported by a fund from the Accelerated Innovation Research Initiative Turning Top Science and Ideas into High-Impact Values (ACCEL) program of the Japan Science and Technology Agency (JST). A portion of this work was supported by a Kakenhi Grant-in-Aid (No. 15H04183) from the Japan Society for the Promotion of Science (JSPS).

■ REFERENCES

(1) Haber, F.; Rossignol, R. L. *Z. Elektrochem. Angew. Phys. Chem.* **1913**, *19*, 53.

(2) Huazhang, L. *Ammonia Synthesis Catalysts—Innovation and Practice*; World Scientific: Singapore, 2013.

(3) Aika, K.; Ozaki, A.; Hori, H. *J. Catal.* **1972**, *27*, 424.

(4) Ozaki, A. *Acc. Chem. Res.* **1981**, *14*, 16.

(5) Dahl, S.; Törnqvist, E.; Chorkendorff, I. *J. Catal.* **2000**, *192*, 381.

(6) Jacobsen, C. J. H.; Dahl, S.; Hansen, P. L.; Tornqvist, E.; Jensen, L.; Topsoe, H.; Prip, D. V.; Moenshaug, P. B.; Chorkendorff, I. *J. Mol. Catal. A: Chem.* **2000**, *163*, 19.

(7) Honkala, K.; Hellman, A.; Remediakis, I. N.; Logadottir, A.; Carlsson, A.; Dahl, S.; Christensen, C. H.; Nørskov, J. K. *Science* **2005**, *307*, 555.

(8) Rarog-Pilecka, W.; Miskiewicz, E.; Szmigiel, D.; Kowalczyk, Z. *J. Catal.* **2005**, *231*, 11.

(9) Gavnholt, J.; Schiøtz, J. *Phys. Rev. B: Condens. Matter Mater. Phys.* **2008**, *77*, 035404.

(10) Aika, K.; Takano, T.; Murata, S. *J. Catal.* **1992**, *136*, 126.

(11) Rosowski, F.; Hornung, A.; Hinrichsen, O.; Herein, D.; Muhler, M.; Ertl, G. *Appl. Catal., A* **1997**, *151*, 443.

(12) Bielawa, H.; Hinrichsen, O.; Birkner, A.; Muhler, M. *Angew. Chem., Int. Ed.* **2001**, *40*, 1061.

(13) Tsai, M. C.; Ship, U.; Bassignana, I. C.; Kuppers, J.; Ertl, G. *Surf. Sci.* **1985**, *155*, 387.

(14) Rao, C. N. R.; Rao, G. R. *Surf. Sci. Rep.* **1991**, *13*, 223.

(15) Hansen, T. W.; Wangner, J. B.; Hansen, P. L.; Dahl, S.; Topsøe, H.; Jacobsen, C. J. H. *Science* **2001**, *294*, 1508.

(16) Larichev, Y. V. *J. Phys. Chem. C* **2011**, *115*, 631.

(17) Szmigiel, D.; Bielawa, H.; Kurtz, M.; Hinrichsen, O.; Muhler, M.; Rarog, W.; Jodzis, S.; Kowalczyk, Z.; Znak, L.; Zielinski, J. *J. Catal.* **2002**, *205*, 205.

(18) Rarog-Pilecka, W.; Szmigiel, D.; Kowalczyk, Z.; Jodzis, S.; Zielinski, J. *J. Catal.* **2003**, *218*, 465.

(19) Matsuishi, S.; Toda, Y.; Miyakawa, M.; Hayashi, K.; Kamiya, T.; Hirano, M.; Tanaka, I.; Hosono, H. *Science* **2003**, *301*, 626.

(20) Kitano, M.; Inoue, Y.; Yamazaki, Y.; Hayashi, F.; Kanbara, S.; Matsuishi, S.; Yokoyama, T.; Kim, S. W.; Hara, M.; Hosono, H. *Nat. Chem.* **2012**, *4*, 934.

(21) Kitano, M.; Kanbara, S.; Inoue, Y.; Kuganathan, N.; Sushko, P. V.; Yokoyama, T.; Hara, M.; Hosono, H. *Nat. Commun.* **2015**, *6*, 6731.

(22) Toda, Y.; Yanagi, H.; Ikenaga, E.; Kim, J. J.; Kobata, M.; Ueda, S.; Kamiya, T.; Hirano, M.; Kobayashi, K.; Hosono, H. *Adv. Mater.* **2007**, *19*, 3564.

(23) Siporin, S. E.; Davis, R. J. *J. Catal.* **2004**, *225*, 359.

(24) Kim, S. W.; Hosono, H. *Philos. Mag.* **2012**, *92*, 2596.

(25) Hayashi, K.; Sushko, P. V.; Ramo, D. M.; Shluger, A. L.; Watauchi, S.; Tanaka, I.; Matsuishi, S.; Hirano, M.; Hosono, H. *J. Phys. Chem. B* **2007**, *111*, 1946.

(26) Matsuishi, S.; Kim, S. W.; Kamiya, T.; Hirano, M.; Hosono, H. *J. Phys. Chem. C* **2008**, *112*, 4753.

(27) Sushko, P. V.; Shluger, A. L.; Hayashi, K.; Hirano, M.; Hosono, H. *Thin Solid Films* **2003**, *445*, 161.

DOI: 10.1021/jacs.5b10145
J. Am. Chem. Soc. 2015, 137, 14517−14524

(28) Matsuishi, S.; Nomura, T.; Hirano, M.; Kodama, K.; Shamoto, S.; Hosono, H. *Chem. Mater.* **2009**, *21*, 2589.
(29) Yoshizumi, T.; Matsuishi, S.; Kim, S. W.; Hosono, H.; Hayashi, K. *J. Phys. Chem. C* **2010**, *114*, 15354.
(30) Sushko, P. V.; Shluger, A. L.; Hirano, M.; Hosono, H. *J. Am. Chem. Soc.* **2007**, *129*, 942.
(31) Jeevaratnam, J.; Glasser, L. S. D.; Glasser, F. P. *Nature* **1962**, *194*, 764.
(32) Kim, S. W.; Matsuishi, S.; Nomura, T.; Kubota, Y.; Takata, M.; Hayashi, K.; Kamiya, T.; Hirano, M.; Hosono, H. *Nano Lett.* **2007**, *7*, 1138.
(33) Vojvodic, A.; Medford, A. J.; Studt, F.; Abild-Pedersen, F.; Khan, T. S.; Bligaard, T.; Nørskov, J. K. *Chem. Phys. Lett.* **2014**, *598*, 108.
(34) Aika, K.; Shimazaki, K.; Hattori, Y.; Ohya, A.; Ohshima, S.; Shirota, K.; Ozaki, A. *J. Catal.* **1985**, *92*, 296.
(35) Hagen, S.; Barfod, R.; Fehrmann, R.; Jacobsen, C. J. H.; Teunissen, H. T.; Chorkendorff, I. *J. Catal.* **2003**, *214*, 327.
(36) Aika, K.; Kumasaka, M.; Oma, T.; Kato, O.; Matsuda, H.; Watanabe, N.; Yamazaki, K.; Ozaki, A.; Onishi, T. *Appl. Catal.* **1986**, *28*, 57.
(37) Hayashi, K.; Matsuishi, S.; Kamiya, T.; Hirano, M.; Hosono, H. *Nature* **2002**, *419*, 462.
(38) Sushko, P. V.; Shluger, A. L.; Hayashi, K.; Hirano, M.; Hosono, H. *Phys. Rev. Lett.* **2003**, *91*, 91.
(39) Kim, S. W.; Miyakawa, M.; Hayashi, K.; Sakai, T.; Hirano, M.; Hosono, H. *J. Am. Chem. Soc.* **2005**, *127*, 1370.
(40) Larichev, Y. V.; Moroz, B. L.; Zaikovskii, V. I.; Yunusov, S. M.; Kalyuzhnaya, E. S.; Shur, V. B.; Bukhtiyarov, V. I. *J. Phys. Chem. C* **2007**, *111*, 9427.

DOI: 10.1021/jacs.5b10145
J. Am. Chem. Soc. 2015, 137, 14517−14524